

Weak-focused acoustic vortex generated by a focused ring array of planar transducers and its application in large-scale rotational object manipulation

Yuzhi Li(李禹志), Peixia Li(李培霞), Ning Ding(丁宁), Gepu Guo(郭各朴), Qingyu Ma(马青玉)†, Juan Tu(屠娟), and Dong Zhang(章东)

Citation: Chin. Phys. B, 2021, 30 (**4**): 044302. DOI: 10.1088/1674-1056/abca1f
Journal homepage: http://cpb.iphy.ac.cn; http://iopscience.iop.org/cpb

What follows is a list of articles you may be interested in

Measuring orbital angular momentum of acoustic vortices based on Fraunhofer's diffraction

Chao-Fan Gong(龚超凡), Jing-Jing Li(李晶晶), Kai Guo(郭凯), Hong-Ping Zhou(周红平)†, and Zhong-Yi Guo(郭忠义)‡

Chin. Phys. B, 2020, 29 (**10**): 104301. DOI: 10.1088/1674-1056/ab9c11

Acoustic radiation force on thin elastic shells in liquid

Run-Yang Mo(莫润阳), Jing Hu(胡静), Shi Chen(陈时), Cheng-Hui Wang(王成会)

Chin. Phys. B, 2020, 29 (**9**): 094301. DOI: 10.1088/1674-1056/ab943e

Pulling force of acoustic-vortex beams on centered elastic spheres based on the annular transducer model

Yuzhi Li(李禹志), Qingdong Wang(王青东), Gepu Guo(郭各朴), Hongyan Chu(褚红燕), Qingyu Ma(马青玉), Juan Tu(屠娟), Dong Zhang(章东)

Chin. Phys. B, 2020, 29 (**5**): 054302. DOI: 10.1088/1674-1056/ab8210

Acoustic radiation force on a multilayered sphere in a Gaussian standing field

Haibin Wang(汪海宾), Xiaozhou Liu(刘晓宙), Sha Gao(高莎), Jun Cui(崔骏), Jiehui Liu(刘杰惠), Aijun He(何爱军), Gutian Zhang(张古田)

Chin. Phys. B, 2018, 27 (**3**): 034302. DOI: 10.1088/1674-1056/27/3/034302

Multiple off-axis acoustic vortices generated by dual coaxial vortex beams

Wen Li(李雯), Si-Jie Dai(戴思捷), Qing-Yu Ma(马青玉), Ge-Pu Guo(郭各朴), He-Ping Ding(丁鹤平)

Chin. Phys. B, 2018, 27 (**2**): 024301. DOI: 10.1088/1674-1056/27/2/024301

Weak-focused acoustic vortex generated by a focused ring array of planar transducers and its application in large-scale rotational object manipulation*

Yuzhi Li(李禹志)[1], Peixia Li(李培霞)[1], Ning Ding(丁宁)[1], Gepu Guo(郭各朴)[1], Qingyu Ma(马青玉)[1,†], Juan Tu(屠娟)[2], and Dong Zhang(章东)[2]

[1] *School of Computer and Electronic Information/School of Artificial Intelligence, Nanjing Normal University, Nanjing* 210023, *China*
[2] *Institute of Acoustics, Nanjing University, Nanjing* 210093, *China*

(Received 14 October 2020; revised manuscript received 5 November 2020; accepted manuscript online 13 November 2020)

Contactless manipulation of multi-scale objects using the acoustic vortex (AV) tweezers offers tremendous perspectives in biomedical applications. However, it is still hindered by the weak acoustic radiation force (ARF) and torque (ART) around the vortex center. By introducing the elevation angle to the planar transducers of an *N*-element ring array, the weak-focused acoustic vortex (WFAV) composed of a main-AV and *N* paraxial-AVs is constructed to conduct a large-scale object manipulation. Different from the traditional focused AV (FAV) generated by a ring array of concave spherical transducers, a much larger focal region of the WFAV is generated by the main lobes of the planar transducers with the size inversely associated with the elevation angle. With the pressure simulation of the acoustic field, the capability of the rotational object driving in the focal plane for the WFAV is analyzed using the ARF and the ART exerted on an elastic ball based on acoustic scattering. With the experimental system built in water, the generation of the WFAV is verified by the scanning measurements of the acoustic field and the capability of object manipulation is also analyzed by the rotational trapping of floating particles in the focal plane. The favorable results demonstrate the feasibility of large-scale rotational manipulation of objects with a strengthened ART and a reduced acousto-thermal damage to biological tissues, showing a promising prospect for potential applications in clinical practice.

Keywords: acoustic vortex, weak-focused, large-scale object manipulation, acoustic scatter, acoustic radiation force

PACS: 43.25.Qp, 43.60.Fg, 43.38.Hz **DOI:** 10.1088/1674-1056/abca1f

1. Introduction

Due to the orbital angular momentum transfer of helical wavefronts, the acoustic vortex (AV)[1–6] has been proved to possess the capability of object manipulation. The center pressure null[7,8] formed by the screw phase dislocation can be applied to form the potential well to trap small objects in a rotation manner. The AV beam can go deeply into tissues[9–11] to manipulate small targets[12–16] as vortex tweezers, exhibiting the application potential in the fields of particle manipulation and drug delivery in biomedical engineering. It was reported that the acoustic radiation torque (ART)[17] of a monochromatic nonparaxial AV beam was proportional to the power absorbed by the object with a factor of l/ω, where l was the topological charge of the AV. To generate an AV with a phase spiral, the phased technology for the point or quasi-point sources was often employed based on acoustic interference. AVs with $l = 1$ and 2 were generated[18,19] using an 8-source array and the OAM transfer was verified by the measurement of the ART exerted on a hanging disk. For the phase-coded approach[20–22] applied to a ring array of N sources, the maximum topological charge of the AV was achieved and the circular distributions of pressure and phase were also discussed. However, the AVs generated by the ring array were along the center axis of the acoustic beam with a low-level trapping force, resulting in an instable axial manipulation of particles.

A spherical transducer array was developed[23,24] to generate AVs and a stable trapping of particles of wavelength order was demonstrated. The rotation speed of particles was adjusted by regulating the amount of time for each direction of the emitted vortex. Whereas, for weak directional transducers with $k_0 b = 3.7$ (product of the wave number k_0 and the transducer radius b), the axial width of the interference area could not be limited effectively by the main lobes. The axially controllable deep-level multiple traps[25] of AVs using directional sources ($k_0 b = 29.32$) were investigated. The main-AV formed by main lobes was far away from the source plane in a divergent manner and the energy was not fully utilized to produce a strong capability of object manipulation. A triangular lattice phased array was reported[26] to generate a focused AV (FAV) with the peak pressure increased up to 3 times that of a non-focalized one. By mounting an acoustic

*Project supported by the National Natural Science Foundation of China (Grant Nos. 11934009, 11974187, and 12004187) and the Natural Science Foundation of Jiangsu Province, China (Grant Nos. BK20161013 and BK20200724).

†Corresponding author. E-mail: maqingyu@njnu.edu.cn

© 2021 Chinese Physical Society and IOP Publishing Ltd

lens on a phased array, a FAV was developed[27] to manipulate objects on a thin film. The clearest experiment concerning the ART on spheres[28] was observed by the simultaneous rotating and trapping of particles. Riaud *et al.*[11] reported that precursor swirling Rayleigh waves could degenerate into AVs after crossing a stack made of a liquid layer and its solid support, creating a localized acoustic trap in a fluid cavity. The inverse problem to design integrated transducers for arbitrary acoustic fields was solved and applied to design an integrated spiraling transducer for AVs. This technology was selective, label-free, biocompatible, flat, easy to miniaturize, and compatible with microfluidic disposable chips, which opened exciting prospects for cell printing and tissue engineering. In order to improve the selectivity and integrability of contactless particle manipulation, the potential of FAV[29] was unleashed by developing the first flat, compact, paired single electrode focalized acoustical tweezers, which relied on spiraling transducers obtained by folding a spherical AV on a flat piezoelectric substrate. The ability to grab and displace micrometric objects in a standard microfluidic environment with unique selectivity was demonstrated. However, due to the small size of the focal zone, the practical application of the FAV is still limited by the weak ART[30] exerted on objects and the possible acousto-thermal damage to biological tissues at the focal center.

In this paper, by introducing the elevation angle to the planar transducers of an N-element ring array, the weak-focused acoustic vortex (WFAV) composed of a main-AV and N paraxial-AVs is constructed to conduct a large-scale rotational manipulation of objects in the focal plane. Compared with the ellipsoidal focal zone formed by the concave spherical transducers, the cone-shaped WFAV generated by the main lobes of the planar sources is much larger with the size inversely associated with the elevation angle. Based on acoustic scattering, the transverse properties and the capacity of rotational object trapping of the WFAV is analyzed in detail. Compare with the FAV, the higher ARF and ART exerted on an elastic ball can be produced by the WFAV in a larger radius. The pressure distribution of the WFAV is confirmed by the experimental scanning measurement in water and the capability of object manipulation in the focal plane is also verified by the rotational capture of particles on the water surface. The favorable results demonstrate the feasibility of large-scale rotational manipulation of objects with a strengthened ART and a reduced acousto-thermal damage to biological tissues. In addition, with a confocal design with a high intensity focused ultrasound (HIFU), the WFAV can be used to improve the therapeutic effect of HIFU therapy with the accumulation of drug particles, which might enable more potentials in clinical applications.

2. Principle and Method

The schematic diagram of the WFAV system is shown in Fig. 1(a). N planar transducers (radius b) are placed evenly on a circumference (array radius R_0) of a sphere (focal length R) with surfaces pointing to the focal center F. The radiation pattern $D(\theta) = |2\mathrm{J}_1(k_0 b\sin\theta)/(k_0 b\sin\theta)|$[24] is produced by the transducer with $k_0 b \gg 1$, where $\mathrm{J}_1(x)$ is Bessel function of the first order and θ is the radiation angle. A narrow main lobe is achieved by the first solution of $D(\theta_{1\mathrm{N}}) = 0$. The elevation angle $\theta_\mathrm{e} = \sin^{-1}(R_0/R)$ is used to describe the tilt direction of the sources. Different from the FAV formed by a ring array of concave spherical transducers with a same focal point, a much larger cone-shaped focal zone can be generated by the main lobes of planar transducers, which is named the WFAV in this study to distinguish from the FAV.

The phase-coded approach[20] is employed to form the AV beam with a controllable topological charge l. The spatial angle and the initial phase of the n-th source are set to $\varphi_n = n(2\pi/N)$ and $\phi_n = nl(2\pi/N)$ for $n = 0$ to $N-1$. As shown in Fig. 1(a), the acoustic pressure at (r,φ,z) produced by the n-th source[25,31] can be calculated by

$$p_n(r,\varphi,z) = \mathrm{i}\omega\frac{\rho_0 q_0 b^2}{2R_n}\left[\frac{2\mathrm{J}_1(k_0 b\sin\theta_n)}{k_0 b\sin\theta_n}\right] \times \exp(\mathrm{i}k_0 R_n - \mathrm{i}\omega t)\exp(\mathrm{i}\varphi_n), \quad (1)$$

where q_0 is the acoustic source strength, R_n and θ_n are the transmission distance and the radiation angle from the n-th source to (r,φ,z). Thus, the acoustic pressure of the AV beam can be achieved as

$$p(r,\varphi,z) = \mathrm{i}\omega\sum_{n=0}^{N-1}\frac{\rho_0 q_0 b^2}{2R_n}\left[\frac{2\mathrm{J}_1(k_0 b\sin\theta_n)}{k_0 b\sin\theta_n}\right] \times \exp(\mathrm{i}k_0 R_n - \mathrm{i}\omega t)\exp(\mathrm{i}\phi_n). \quad (2)$$

Therefore, the cone-shaped WFAV can be formed by the main lobes for $\theta_n < \theta_{1\mathrm{N}}$. Although many on-axis or off-axis sub-AVs can also be generated by the side lobes ($\theta_n > \theta_{1\mathrm{N}}$), they can be neglected in practical applications due to the low-level acoustic pressure.

As we know, the acoustic gradient force (AGF) based on the Gor'kov potential is often used to estimate the ARF acting on the particles with the size much smaller than the wavelength. However, the influence of acoustic scattering by the particles of a bigger size should be taken into account in practical applications. Therefore, a general derivation of the ARF exerted on an elastic ball in the WFAV is studied based on acoustic scattering to achieve a more accurate analysis of the rotational object manipulation. As shown in Fig. 1(b), an elastic ball with the radius a is located at an arbitrary point, which is positioned at the new origin O' in the spherical coordinates with the radius, the polar and azimuthal angles of r', θ', and

φ'. Thus, the scattered pressure[31] at (r', θ', φ') radiated from S_p on the transducer surface can be written as

$$p(r', \theta', \varphi') = \sum_{l=0}^{\infty} \left\{ \left[\frac{\mathrm{j}_l'(k_0 a) + \mathrm{i}\beta_l \mathrm{j}_l(k_0 a)}{\mathrm{h}_l'(k_0 a) + \mathrm{i}\beta_l \mathrm{h}_l(k_0 a)} \right] \mathrm{h}_l(k_0 r') - \mathrm{j}_l(k_0 r') \right\} \times q_0 \rho_0 c_0 k_0^2 \frac{(2l+1)}{4\pi} \mathrm{h}_l(k_0 r_p) \mathrm{P}_l(\cos\theta''), \quad a < r' < r_\mathrm{s}, \tag{3}$$

where $\mathrm{j}_l(x)$, $\mathrm{h}_l(x)$, and $\mathrm{P}_l(x)$ are the spherical Bessel function, the spherical Hankel function of the first kind, and the Legendre polynomial of l order, respectively. The acoustic contrast factor $\beta_l = \mathrm{i} \cdot \rho_0 c_0 \mathrm{j}_l'(k_\mathrm{s} a) / [\rho_\mathrm{s} c_\mathrm{s} \mathrm{j}_l(k_\mathrm{s} a)]$ is determined by the impedance difference between the elastic ball and surrounding water, where ρ_s, c_s, and k_s are the density, the acoustic speed, and the wave number of the ball. Therefore, the scattered pressure at (r', θ', φ') in the WFAV can be calculated by

$$p(r', \theta', \varphi') = \sum_{n=0}^{N-1} \sum_{l=0}^{\infty} \left\{ \left[\frac{\mathrm{j}_l'(k_0 a) + \mathrm{i}\beta_l \mathrm{j}_l(k_0 a)}{\mathrm{h}_l'(k_0 a) + \mathrm{i}\beta_l \mathrm{h}_l(k_0 a)} \right] \mathrm{h}_l(k_0 r') - \mathrm{j}_l(k_0 r') \right\} \times q_0 \rho_0 c_0 k_0^2 \exp(\mathrm{i}\phi_n) \frac{(2l+1)}{4\pi} \times \int_0^{2\pi} \int_0^b \mathrm{h}_l(k_0 r_p) \mathrm{P}_l(\cos\theta'') \cdot r_{bn} \cdot \mathrm{d}r_{bn} \mathrm{d}\varphi_{pn}, \tag{4}$$

where r_{bn} and φ_{pn} are the integral variables of the n-th transducer and r_p is the distance from S_p to (r', θ', φ'). Then the ARF[32–37] exerted on the ball can be obtained by

$$\boldsymbol{F}_{S_0} = \int_{S_0} \left\langle \frac{\rho_0 (v \cdot v)}{2} \boldsymbol{n} - \frac{p_{S_0}^2}{2\rho_0 c_0^2} \boldsymbol{n} - \rho_0 (\boldsymbol{n} \cdot \boldsymbol{v}) \boldsymbol{v} \right\rangle \cdot \mathrm{d}S, \tag{5}$$

where $p_{S_0} = p(a, \theta', \varphi')$, $\boldsymbol{n}$ is the unit vector of the integral surface, the acoustic velocity on the ball surface is $\boldsymbol{v} = \nabla p_{S_0} / (\mathrm{i}\omega\rho_0)$ and $\langle \cdot \rangle$ is the time-averaged calculation over one period. Assuming the ball is placed on the y axis with the offset $\mathrm{d}y$ from the origin O, the ART exerted on the ball can be calculated by

$$\boldsymbol{r} \times \boldsymbol{F}_x = -\left(\mathrm{d}y \boldsymbol{F}_{S_0} \cdot \boldsymbol{e}_x\right) \boldsymbol{e}_z, \tag{6}$$

where $\boldsymbol{e}_x$ and $\boldsymbol{e}_z$ are the unit vectors along the corresponding directions.

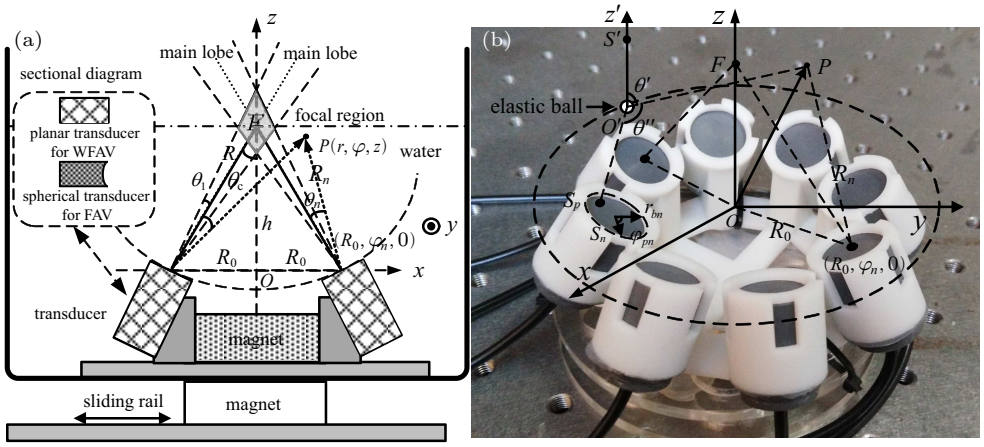


Fig. 1. (a) Schematic diagram of the WFAV system, and (b) the analysis of the acoustic scattering on an elastic ball located in the WFAV generated by an experimental ring array of 8 transducers with the elevation angle of 30°.

3. Numerical and experimental studies

Numerical studies are conducted for an 8-source ring array with $R = 60$ mm, $b = 7$ mm, and $\theta_\mathrm{c} = 30°$ at $f = 1$ MHz in water, the density and the acoustic speed in water are set to be $\rho_0 = 1000$ kg/m^3 and $c_0 = 1500$ m/s. Cross-sectional distributions of pressure and phase for the WFAV with $l = 1$ at the focal distance ($z = 52.0$ mm) are plotted in Figs. 2(a1) and 2(a2). Concentric pressure circles with an obvious pressure zero at the center is clearly displayed in Fig. 2(a1). The radii of the pressure peak and valley of the main-AV are about 0.85 mm and 1.8 mm, respectively. The main-AV in $r < 1.8$ mm is proved by the conspicuous clockwise phase spiral from $-\pi$ to π in Fig. 2(a2), and an expanded AV is also identified by the phase spiral in $r < 3.7$ mm. Meanwhile, eight phase spirals evenly distributed on the circumference ($r = 4.8$ mm) demonstrate the occurrence of eight paraxial-AVs with the radius of 1.8 mm. Due to the interference of the main lobes of the planar transducers on the ring array, the number of paraxial-AVs is equal to that of the sources. In addition, obvious off-axis sub-AVs formed by side lobes can also be observed by the phase spirals in $r > 6.6$ mm. Thus, the maximum radial distance of about 6.6 mm can be regarded as the radius of the WFAV, which is 4 times larger than the wavelength. The axial pressure profile in Fig. 2(a3) shows a large-scale WFAV around the focal center. The main-AV and paraxial-AVs symmetrically distributed around the beam axis agree well with the cross-sectional distributions in Figs. 2(a1) and 2(a2). Whereas, several off-axis sub-AVs outside the WFAV are too low to be identified.

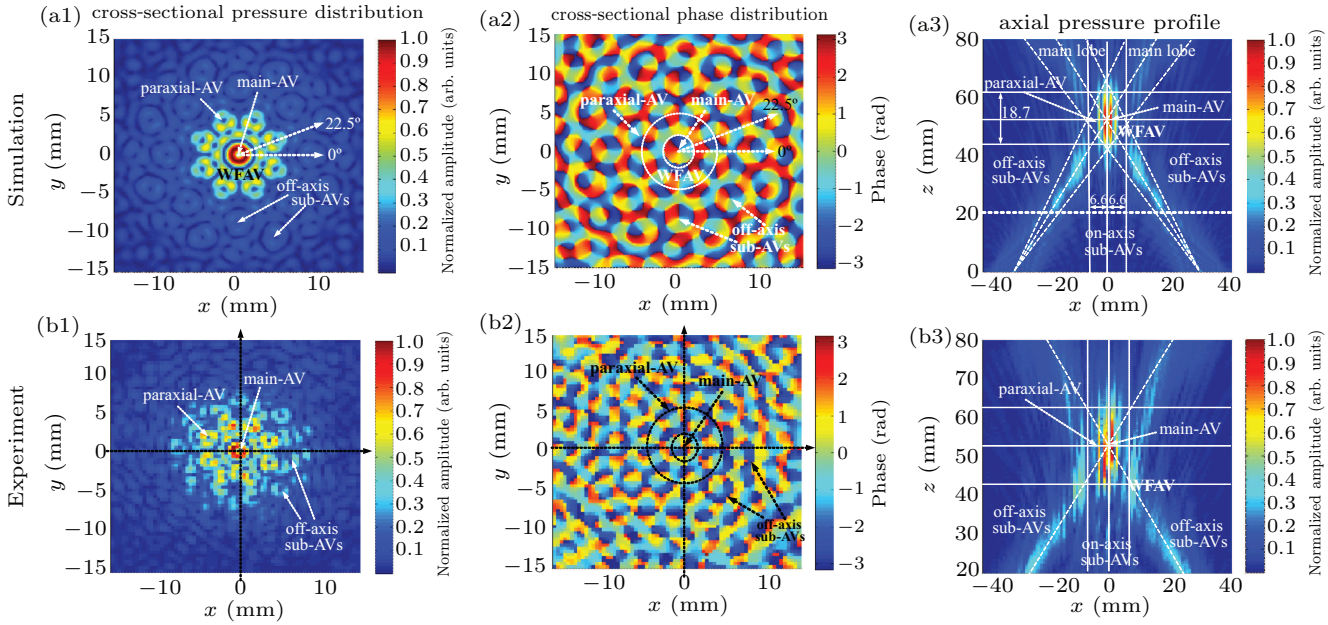


Fig. 2. Numerical (line 1) and experimental (line 2) cross-sectional distributions of (a1, b1) pressure and (a2, b2) phase in the focal plane at $z = 52.0$ mm, and (a3, b3) the corresponding axial pressure profiles.

The experimental ring array of eight planar transducers with the elevation angle of 30° was fabricated as displayed in Fig. 1(b). The array bracket was manufactured by three-dimensional (3D) printing using the photopolymer material, and the planar transducers (radius 7 mm, center frequency 1 MHz) made of PZT were commercially customized by Chongqing Haifu Medical Technology Co. Ltd. An 8-channel phase-coded driving circuit[19,29] made by the direct digital synthesis (DDS) devices and the high-frequency power amplifiers was used to excite the transducers with the phase difference of $\pi/4$. The acoustic pressure was scanned by a needle hydrophone (Onda HNR-1000, Onda Corporation, USA) using two step motors (Newport M-ILS250, Newport Corporation, USA) at the step of 0.1 mm, and collected by the digital oscilloscope (Agilent DSO9064A, Agilent Technologies, USA). To reduce the influence of the near-field interference, the axial measurement distance was set from 20 mm to 80 mm. Besides, two magnets mounted inside and outside the water tank were used to conduct a contactless linear motion control of the ring array.

The experimental cross-sectional distributions of pressure and phase in the focal plane at $z = 52.0$ mm are illustrated in Figs. 2(b1) and 2(b2), which are in good agreements with the simulations in Figs. 2(a1) and 2(a2). For the possible experimental errors in scanning measurements, the vortex center (indicated by the intersection of the axes) of the WFAV deviates slightly from the origin as shown in Fig. 2(b1). As indicated by the arrows, a main-AV and eight paraxial-AVs located around are clearly displayed with obvious pressure circles, which are verified by the corresponding phase spirals as shown in Fig. 2(b2). Meanwhile, several off-axis sub-AVs outside the WFAV can also be identified in Figs. 2(a) and 2(b). In addition, the experimental axial profile in Fig. 2(b3) in terms of the location and size of the main-AV and paraxial-AVs consists qualitatively with the simulation in Fig. 2(a3).

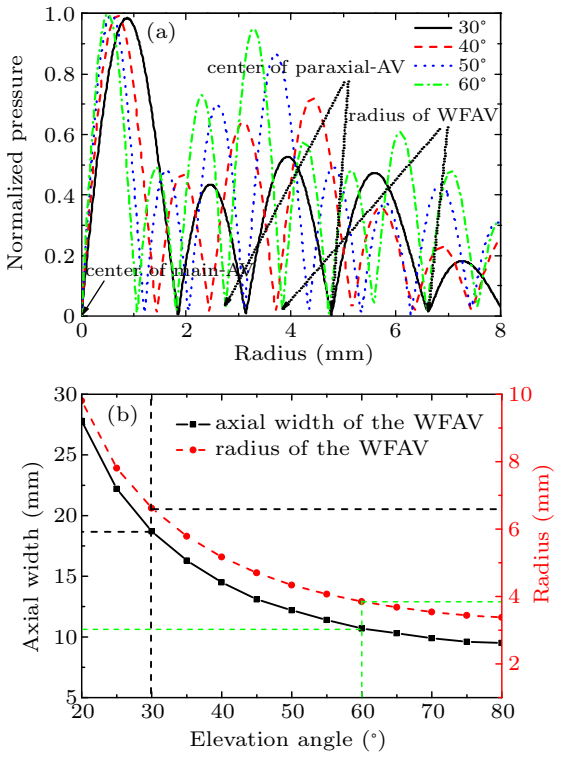


Fig. 3. (a) Normalized radial pressure distributions of WFAV for the transducer arrays with different elevation angles, and (b) the elevation angle dependences of the axial width and the radius of the WFAV.

Also as indicated by the arrows in Fig. 2(a1), normalized radial pressure distributions in the focal plane at $\varphi = 22.5°$ for the ring arrays of planar transducers with various elevation angles are plotted in Fig. 3(a). Although there are several pressure valleys along the radial direction, the vortex centers of the

main-AV and paraxial-AVs are located at the 1st and 4th pressure valleys of $r = 0$ mm and 4.8 mm, and the radius of the WFAV is positioned at the 5-th pressure valley of $r = 6.6$ mm. It shows that the radii of the main-AV and paraxial-AVs decrease accordingly for a larger elevation angle. As plotted in Fig. 3(b), the radius in the focal plane and the axial width (−6 dB attenuation) of the WFAV exhibit a similar decreasing tendency with respect to the elevation angle. When the elevation angle is enhanced from 20° to 80°, the radius of the WFAV decreases from 9.8 mm to 3.4 mm with a declined axial width from 27.8 mm to 9.5 mm. For the array with $\theta_c = 30°$, the axial width (18.7 mm) and the radius (6.6 mm) are proved by the similar sizes as indicated in Fig. 2(a3). Thus, the size of the WFAV can be controlled accurately by the elevation angle of the transducers, and a more concentrated WFAV with a smaller main-AV can be formed by a bigger elevation angle.

To make a precise comparison with the WFAV, the model of the traditional FAV is developed by replacing each planar transducer with a concave spherical one with the conceptual diagram as shown in Fig. 1(a). The focal length of the concave spherical transducers is set to $R = 60$ mm with the height of the spherical cap of 0.4 mm to ensure the same surface area as the planar one. By applying the phase difference to the ring array, the FAV can be generated around the focus. Cross-sectional distributions of pressure and phase in the focal plane of the FAV with $l = 1$ are illustrated in Figs. 4(a) and 4(b), and the corresponding axial pressure profile is also presented in Fig. 4(c). The FAV featured by the obvious concentric circles with a pressure null at the center is clearly displayed in Fig. 4(a) and the formation of the FAV in $r < 1.8$ mm is proved by the perfect phase spiral around the center in Fig. 4(b). The circular pressure distributions of eight paraxial-AVs are incomplete with the pressure obviously lower than that of the FAV. In addition, the acoustic pressures of the off-axis sub-AVs are too low to be identified in Fig. 4(a). Compared with the axial profile of the WFAV in Fig. 2(a3), only the main-AV around the focus can be observed in Fig. 4(c). Therefore, due to the focusing of the concave spherical transducers, the acoustic power is more concentrated in the FAV around the focal center.

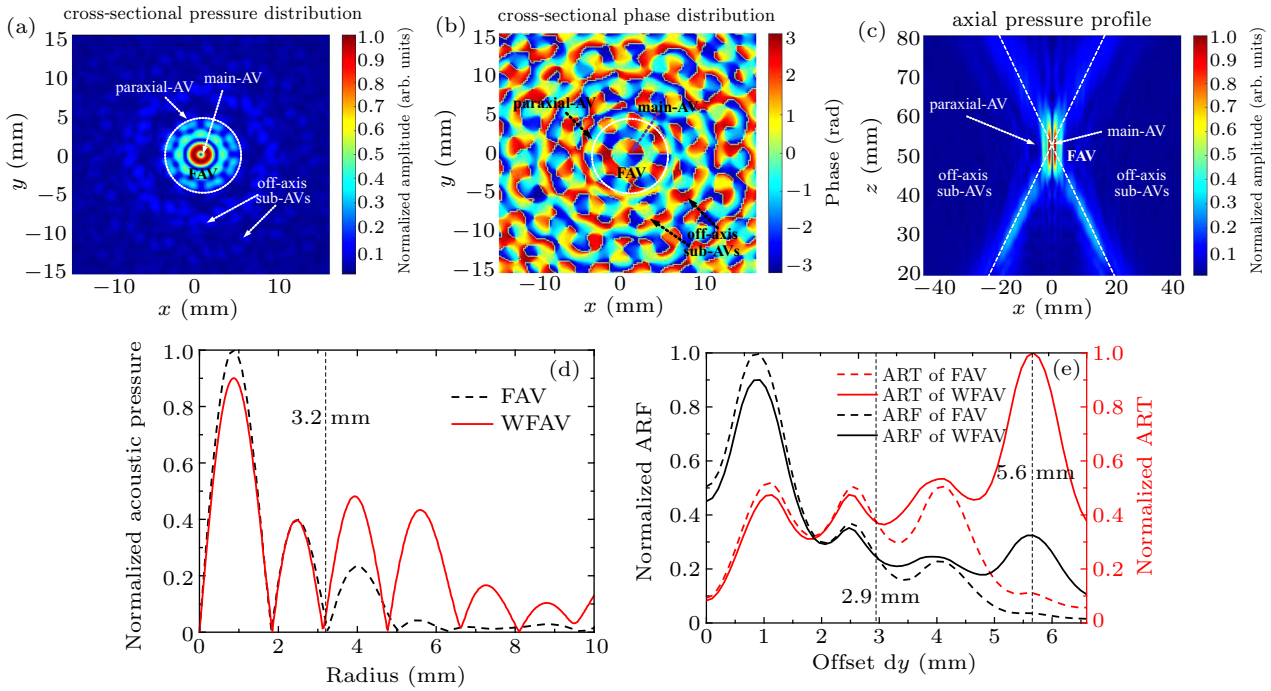


Fig. 4. Cross-sectional distributions of (a) pressure and (b) phase in the focal plane, and (c) the corresponding axial pressure profile of the FAV with $l = 1$ generated by the ring array of 8 concave spherical transducers. (d) Normalized radial pressure distributions of the WFAV and the FAV, and (e) the offset dependences of the tangential ARF and the corresponding ART exerted on an elastic ball in the WFAV and the FAV.

As plotted in Fig. 4(d), the normalized radial pressure distribution of the WFAV at $\varphi = 22.5°$ in the focal plane is simulated to analyze the driving capability of the WFAV, and the corresponding distribution of the FAV is also provided for comparison. It shows that the pressure peak of the FAV is a little higher than that of the main-AV of the WFAV at $r = 0.9$ mm, whereas, the pressure peak of the FAV decreases with the increase of the radius. When $r > 3.2$ mm, the 3rd and the 4th acoustic pressure peak of the FAV is obviously lower than that of the WFAV, meaning that no obvious paraxial-AVs can be formed in the FAV. Then, the offset dependences of the tangential ARF and the corresponding ART exerted on the elastic ball ($a = 0.5$ mm) in the WFAV are compared with those of the FAV. The comparisons plotted in Fig. 4(e) show that the tangential ARF of the FAV is stronger than that of the WFAV in the center region. When the ball is moved farther to $dy > 2.9$ mm, a higher tangential ARF of the WFAV is produced, especially for the existence of paraxial-AVs at

$dy = 5.6$ mm. Meanwhile, the corresponding ART generated by the FAV is a little higher than that of the WFAV when the ball is located at the central region in $dy < 2.9$ mm. With the further increase of dy, the ART of the WFAV enhances rapidly with the maximum value at $dy = 5.6$ mm, which is about 9 times that of the FAV. Therefore, the improved capability of large-scale object manipulation can be created for the WFAV due to the higher ARF when 2.9 mm$< r <$ 6.6 mm.

In order to further analyze the capability of object manipulation, the acoustic pressure scattered by the elastic ball with $a = 0.5$ mm, $\rho_s = 980$ kg/m^3, and $c_s = 2300$ m/s is simulated. Supposing the elastic ball is located eccentrically at (0, 0.8) mm in the focal plane at $z = 52.0$ mm, cross-sectional pressure distributions scattered by the ball radiated from each transducer are illustrated in Figs. 5(a)–5(h). Obvious pressure fluctuations indicate the acoustic diffraction and reflection of the elastic ball. By further considering the initial phases of the sources, distributions of pressure and phase of the WFAV are illustrated in Figs. 5(i) and 5(j). The acoustic pressure on the left side of the ball is obviously higher than that on the right side as plotted in Fig. 5(i), creating the ARF (about 8.2 nN, white arrows) along the normal direction of the helical wavefronts as shown in Fig. 5(j). The ARF produced by the WFAV on the elastic ball deviates slightly from the tangent direction with a radial component towards the vortex center, which produces in an inward rotation driving for the ball. The direction of the inward object rotation is determined by the tangential and radial components of the ARF in the transverse plane. Thus, by considering the role of the arm, a strengthened ART can be produced by the WFAV, which is beneficial to the rotational manipulation of objects in a large scale.

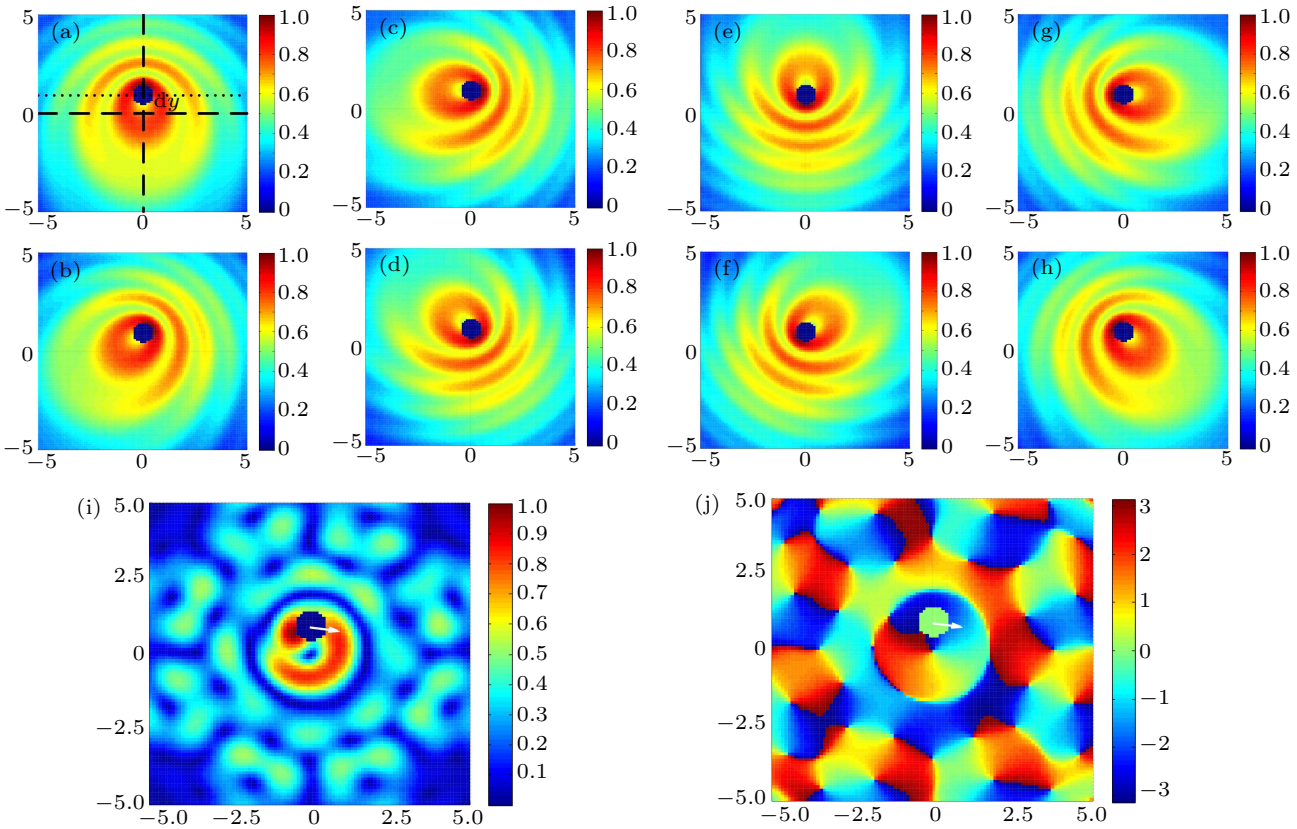


Fig. 5. (a)–(h) Cross-sectional pressure distributions scattered by the elastic ball radiated from each source of the transducer array independently, and the distributions of (i) pressure and (j) phase of the WFAV with the arrows representing the amplitude and direction of the ARF (For the experimental surface pressure of 45 kPa on each planar transducer, the pressure peak of the WFAV reaches 310 kPa and produce an ARF of nN-level in the focal plane).

The performance of object manipulation of the WFAV is demonstrated by the experimental rotation and movement of the center accumulated polyethylene particles ($a = 0.5$ mm). For the axial radiation force of nN level is too low to be measured, particles floating on the transparent surface of water were often used to study the characteristics of the rotational trapping in the focal plane at $z = 52$ mm to improve the observation effect. Due to the action of the ARF, particles rotate anticlockwise around the center with an obvious accumulation in a circular distribution of the radius of 6.0 mm in Fig. 6(a). For the WFAV is formed by the interference of the main lobes of the transducers, particles inside the WFAV can be easily driven by the strong ARF produced by the main-AV and the paraxial-AVs as shown in Fig. 2. While, although the off-axis AVs can also be formed by the side lobes outside the WFAV, the acoustic power is too low to driven the particles. Therefore, as observed in the Supplementary video I, particles inside the central area with the radius of about

6.0 mm are gathered to the center in a rotation manner, while the ones outside keep a steady state. A clear circular demarcation (6.0 mm$< r <$ 8.0 mm) between the rotating and static particles agree well with the theoretical radius of the WFAV (6.6 mm). By moving the outside magnet along the sliding rail, particles ($r <$ 3.0 mm) trapped by the WFAV in Fig. 6(b) move along with the ring array (Supplementary video II), demonstrating the capability of the real-time particle trapping in a large scale.

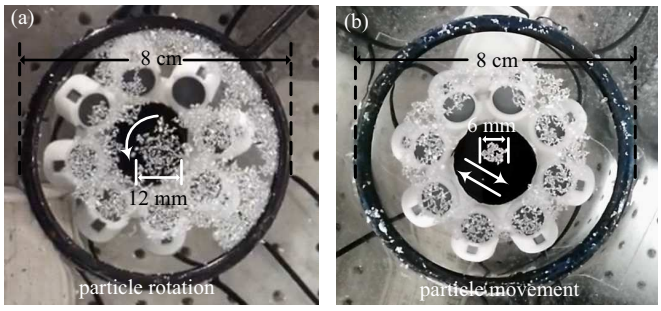


Fig. 6. Experimental pictures of (a) rotation and (b) movement of the accumulated polyethylene particles in the WFAV.

4. Discussion

For the ring array of eight planar transducers with a given R_0, the shape and size of the WFAV can be adjusted by the elevation angle θ_c, which is also limited by the configuration of the array and size of the transducers. For $\theta_c = 90°$, all the transducers are positioned in the source plane with the surfaces pointing to the center, and an octagon AV at the center inside the array can be formed by the main lobes of the sources. However, for this case, the object to be manipulated should be placed in the source plane without axial operation depth, which would limit the practical application of AV manipulations. While, for the specific angle of $\theta_c = 0°$, the model is the traditional ring array[25] with the transducer faces perpendicular to the beam axis, and the main-AV can be generated by the main lobes of the sources. However, due to the directivity of the transducers, the main-AV is far away from the source plane in a divergent manner, and the acoustic energy cannot be fully utilized to produce a strong capability of object manipulation.[38] Thus, the WFAV is proposed to shorten the axial distance of the focal zone with an improved capability of object manipulation.

In the present study, the WFAV is generated by the ring array of eight planar transducers with the focal length $R =$ 60 mm and the source radius $b = 7$ mm. To avoid the acoustic reflection by the transducers, the maximum elevation angle of 82.2° should be taken into account based on the geometry configuration. By considering the appropriate operation depth (axial distance) of the WFAV, the elevation angle from 20° to 80° is studied in simulations. Meanwhile, the formation of the WFAV is also affected by the directivity of the planar piston transducers. According to the previous conclusion,[25] a narrower main lobe with a stronger radiation pattern can be produced by a planar transducer with a bigger $k_0 b$. Since the WFAV is formed by the interference of the main lobes of the planar piston sources, a more concentrated WFAV of smaller radial and axial widths can be generated by the transducers of a bigger $k_0 b$. In addition, for the geometry configuration of a fixed R_0 and θ_c in this study, the maximum radius of the planar transducers is determined by the source number as $b_{\max} = R_s \sin\left(\theta_{adj}/2\right) / \sin\left(\theta_{adj}\right)$, where $R_s = 2R_0 \sin(\pi/N)$ and $\cos\theta_{adj} = [\cos(2\pi/N) + \cot^2\theta_c]/(1+\cot^2\theta_c)$.

In order to obtain the accurate acoustic pressure for the WFAV, the laser vibrometer (Polytec OFV-503, Polytec Company, German) was used to measure the acoustic velocity on the planar transducer surface. By adjusting the experimental acoustic velocity on each transducers surface to 30 mm/s, the source pressure was about 45 kPa and the pressure peak of the WFAV reached 310 kPa by the acoustic focusing, producing an nN-level ARF in the focal plane. For the acoustic energy used in particle manipulations, the maximum pressure was less than MPa, and the nonlinear effect of the WFAV and the acoustothermal effect to biological tissues[39] were neglected. However, by further increasing the source pressure to achieve a pressure peak over MPa for the WFAV, the nonlinear effect should be considered to achieve a more accurate calculation of the ARF for object manipulations.

As we know, the axial ARF along the center axis of an acoustic beam mainly works as the positive force to push particles away from the source plane. However, for an AV beam with a pressure null at the center, the negative force[40,42] exerted on a particle along the center axis is easy to generate at appropriate axial distances. The axial performance of a FAV[27] generated by a transducer array and a concave acoustic lens was studied by Baresch *et al.*, and it was proved that the axial ARF was positive inside the beam focus and negative outside as the pushing and pulling forces. The particle reached an axial equilibrium position when the negative ARF balanced the positive one. In addition, Marzo *et al.*[24] demonstrated that the FAV was able to stably trap and effectively control the rotational speed of levitated samples by the independently tunable trapping forces and OAM. The radial and axial ARFs centered on the focus proved the existence of the ARF zero along the beam axis of the FAV. Thus, in order to improve the observation effect in water, objects floating on the water surface were often used to study the characteristics of rotational trapping in the focal plane without considering the axial ARF due to the force balance in the direction of gravity. By applying the holographic acoustic tweezers[43] of AVs using two 256-element phased arrays, the rotations of soap bubbles in opposite directions on the water surface were realized by Marzo and Drinkwater. Therefore, by considering the similar distributions of the WFAV and the FAV, the focal plane on

the water surface with an axial radiation force balance in the direction of gravity can be treated as the optimized position to study the performance of the stable object trapping in the transverse plane.

Although the experiments of particle rotation and movement provide the evidence for the WFAV, there are still some differences between the particle distributions and the theoretical expectations. Due to the electrostatic interaction, obvious particle aggregations are formed on the water surface. Only the rotation of the agglomerated particles as a whole is observed in the supplementary videos because the ARF of main-AV is much larger than of the paraxial-AVs. Meanwhile, independent rotations of several particles can also identified around the centers of the paraxial-AVs. Meanwhile, compared with the WFAV, the acoustic pressure of the off-axis sub-AVs is much smaller and the ARF is too low to produce particle rotation. The clear circular demarcation without particles between the paraxial-AVs and the off-axis sub-AVs in 6.0 mm$< r <$ 8.0 mm is produced by the inward trapping force inside the WFAV and the outward gradient force outside along the radial direction. In addition, the high-intensity focused ultrasound (HIFU)[39] can be used to treat tumors using the thermal ablation of the focused ultrasound energy without the synergy of drug particles. Thus, with a confocal design as shown in Fig. 7, the ring array with the hollow structure can be equipped around a HIFU transducer to form a WFAV covering the elliptical focal zone of thermal ablation. Combined with the effect of large-scale particle trapping, the WFAV can be applied to improve the therapeutic effect of tumor treatments during HIFU therapy with the accumulation of drug particles, which might enable more potentials in medical applications.

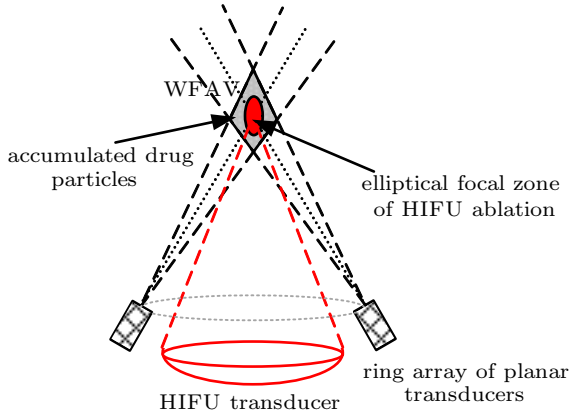


Fig. 7. Sketch map of the combined application of the WFAV during HIFU therapy.

As the conventional AV, objects with the size smaller than the radius of the WFAV can be captured stably, which is determined by the structure of the ring array and the topological charge. For the configuration of the system in this study, the radius (6.6 mm) of the WFAV with $l = 1$ is 4 times larger than the wavelength. Therefore, objects of nm, μm, and mm scales can be manipulated stably by the WFAV, showing a great potential in multi-scale object trapping, especially for bio-particles or drug particles in biomedical applications. As presented in the principle section, the scattered acoustic pressure and the corresponding ARF of the elastic ball are also impacted by β_l in Eq. (4), which is determined by the impedance difference between the elastic ball and surrounding water. The particles with a negative acoustic contrast factor[44,45], *e.g.*, the polydimethylsiloxane (PDMS) microparticles,[46] can migrate transversely with the pressure gradient towards the area of a high pressure, and they are hardly to be accumulated to the center by the WFAV. Therefore, only the regular particles with a positive acoustic contrast factor can be manipulated by the WFAV.

5. Conclusion

By introducing the elevation angle to the planar transducers of an N-element ring array, the WFAV is constructed to conduct a controllable rotational object manipulation in a large scale. Compared with the traditional FAV produced by concave spherical transducers, a much larger scope of the WFAV composed of a main-AV and N paraxial-AVs can be generated with the size inversely associated with the elevation angle. The inward object rotation is demonstrated by the ARF and the ART exerted on an elastic ball based on acoustic scattering. The WFAV generated by an 8-source ring array is verified by the scanning measurement of the acoustic field, and the capability of object manipulation is proved by the rotational trapping of floating particles on the water surface in the focal plane. The favorable results demonstrate that the WFAV is applicable in a large-scale object manipulation with a strengthened ART, exhibiting promising perspectives in medical applications.

References

[1] Hefner B T and Marston P L 1999 *J. Acoust. Soc. Am.* **106** 3313
[2] Thomas J L and Marchiano R 2003 *Phys. Rev. Lett.* **91** 244302
[3] Marchiano R and Thomas J L 2005 *Phys. Rev. E* **71** 066616
[4] Lekner J 2006 *J. Acoust. Soc. Am.* **120** 3475
[5] Marchiano R 2008 *Phys. Rev. E* **77** 016605
[6] Lee C, Jeong J S, Hwang J Y, Lee J and Shung K K 2014 *Appl. Phys. Lett.* **104** 244107
[7] Ashkin A, Dziedzic J M and Yamane T 1987 *Nature* **330** 769
[8] Ashkin A and Dziedzic J M 1989 *Proc. Nadl. Acad. Sci. USA* **86** 7914
[9] Li Y, Lee C, Chen R, Zhou Q and Shung K K 2014 *Appl. Phys. Lett.* **105** 173701
[10] Chen K, Wu M, Guo F, Li P, Chan C, Mao Z, Li S, Ren L, Zhang R and Huang T J 2016 *Lab. Chip* **16** 2636
[11] Riaud A, Baudoin M, Matar O B, Becerra L and Thomas J L 2017 *Phys. Rev. Appl.* **7** 024007
[12] Kang S T and Yeh C K 2010 *IEEE Trans. Ultrason. Ferroelectr. Freq. Contr.* **57** 1451
[13] Baresch D, Thomas J L and Marchiano R 2013 *J. Appl. Phys.* **113** 184901
[14] Skeldon K D, Wilson C, Edgar M and Padgett M J 2008 *New J. Phys.* **10** 013018

[15] Courtney C R P, Demore C E M, Wu H, Grinenko A, Wilcox P D, Cochran S and Drinkwater B W 2014 *Appl. Phys. Lett.* **104** 154103

[16] Marston P L 2007 *J. Acoust. Soc. Am.* **122** 3162

[17] Zhang L and Marston P L 2011 *Phys. Rev. E* **84** 065601

[18] Volke-Sepulveda K, Santillán A O and Boullosa R R 2008 *Phys. Rev. Lett.* **100** 024302

[19] Santillán A O and Volke-Sepulveda K 2009 *Am. J. Phys.* **77** 209

[20] Yang L, Ma Q, Tu J and Zhang D 2013 *J. Appl. Phys.* **113** 154904

[21] Zheng H, Gao L, Ma Q, Dai Y and Zhang D 2014 *J. Appl. Phys.* **115** 084909

[22] Gao L, Zheng H, Ma Q, Tu J and Zhang D 2014 *J. Appl. Phys.* **116** 024905

[23] Marzo A, Seah S A, Drinkwater B W, Sahoo D R, Long B and Subramanian S 2015 *Nat. Commun.* **6** 8661

[24] Marzo A, Caleap M and Drinkwater B W 2018 *Phys. Rev. Lett.* **120** 044301

[25] Li Y, Guo G, Ma Q, Tu J and Zhang D 2017 *J. Appl. Phys.* **121** 164901

[26] Pazos-Ospina J F, Quiceno F, Ealo J L, Muelas R D and Camacho J 2015 *Phys. Procedia* **70** 183

[27] Baresch D, Thomas J L and Marchiano R 2016 *Phys. Rev. Lett.* **116** 024301

[28] Baresch D, Thomas J L and Marchiano R 2018 *Phys. Rev. Lett.* **121** 074301

[29] Baudoin M, Gerbedoen J C, Riaud A, Matar O B, Smagin N and Thomas J L 2019 *Sci. Adv.* **5** eaav1967

[30] Li Y, Guo G, Tu J, Ma Q, Guo X, Zhang D and Sapozhnikov O A 2018 *Appl. Phys. Lett.* **112** 254101

[31] Cheng J 2011 *Principles of Acoustics* (Beijing: Science Express) pp. 247–270

[32] Lee C P and Wang T G 1993 *J. Acoust. Soc. Am.* **93** 1637

[33] Silva G T, Chen S, Greenleaf J F and Fatemi M 2005 *Phys. Rev. E* **71** 056617

[34] Zhang P, Li T, Zhu J, Zhu X, Yang S, Wang Y, Yin X and Zhang X 2014 *Nat. Commun.* **5** 4316

[35] Kido T, Hasegawa T and Okamura N 2004 *Acoust. Sci. Technol.* **25** 439

[36] Sapozhnikov O A and Bailey M R 2013 *J. Acoust. Soc. Am.* **133** 661

[37] Ghanem M A, Maxwell A D, Sapozhnikov O A, Khokhlova V A and Bailey M R 2019 *Phys. Rev. Appl.* **12** 044076

[38] Wang Q, Li Y, Ma Q, Guo G, Tu J and Zhang D 2018 *J. Appl. Phys.* **123** 034901

[39] Li Y, Tao C, Ma Q, Guo G, Zhang D and Hu J 2018 *J. Appl. Phys.* **124** 214905

[40] Marston P L 2007 *J. Acoust. Soc. Am.* **122** 3162

[41] Mitri F G 2009 *J. Phys. A Math. Theor.* **42** 245202

[42] Li Y, Ma Q, Guo G, Tu J and Zhang D 2020 *Chin. Phys. B* **29** 054302

[43] Marzo A and Drinkwater B W 2019 *Proc. Nadl. Acad. Sci. USA* **116** 84

[44] Silva G T and Baggio A L 2015 *Ultrason.* **56** 449

[45] Melde K, Mark A G, Qiu T and Fischer P 2016 *Nature* **537** 518

[46] Meng L, Cai F, Li F, Zhou W, Niu L and Zheng H 2019 *J. Phys. D: Appl. Phys.* **52** 273001